Comparison of laboratory and numerically observed scalar fields of an internal wave attractor

Jeroen Hazewinkel[*,a,b,c], Nicolas Grisouard[d], Stuart B. Dalziel[a]

[a] *Department of Applied Mathematics and Theoretical Physics, University of Cambridge, Wilberforce Road, Cambridge CB3 0WA, UK*
[b] *Centre for Mathematics and Computer Sciences, P.O. Box 94079, NL-1090 GB Amsterdam, The Netherlands*
[c] *Royal Netherlands Institute for Sea Research, P.O. Box 59, 1790 AB Texel, The Netherlands*
[d] *Laboratoire des Écoulements Géophysiques et Industriels, UJF/CNRS/G-INP, BP 53, 38041 Grenoble cedex 9, France*

Abstract

Observations of internal gravity wave beams are frequently accompanied by theory that is purely two-dimensional, or two-dimensional numerical models. Although qualitative agreement between such models and laboratory experiments has been demonstrated, quantitative comparison has only been possible in a limited range of cases. Here, we present a quantitative comparison for internal wave attractors in the laboratory and a two-dimensional non-hydrostatic numerical model. To make a closer connection with previous theoretical work, the experimental and numerical results are presented in terms of the streamfunction and density perturbation, rather than the measured velocity and density gradient fields. The streamfunction is commonly used in the two-dimensional descriptions, e.g. to predict spatial patterns found in an enclosed stratified fluid in the laboratory. We demonstrate that, although the laboratory experiment in a narrow tank is only semi-two-dimensional, the flow is well described by two-dimensional internal wave theory and the numerical model reproduces quantitatively comparable attractors. The observed streamfunction field is compared with theoretical predictions, addressing an open question on the form of the streamfunction for internal wave attractor in a trapezoidal domain. The streamfunction has a simple spatial structure with sharp gradients at the attractor separating regions of nearly constant value outside the attractor.

Keywords: Stratified fluids – Internal waves – Attractors – MIT-gcm – Synthetic schlieren

[*] Corresponding author, presently at Scripps Institute of Oceanography, University of California, San Diego
Email address: jhazewinkel@ucsd.edu (Jeroen Hazewinkel)

1. Introduction

Internal wave attractors can arise in stably stratified fluids in a confined domain [13] and are observed in the laboratory [12]. In a trapezoidal tank of uniform width with one sloping end-wall, internal waves reflect from the sloping wall into the domain and are focused towards an attractor. Repeated reflection from the sloping wall leads to an energy cascade to the higher wave numbers [7]. With a steady forcing at large scales, a balance is reached between the energy cascade and dissipation at the viscous scale, observed as a steady state internal wave attractor. The steady state internal wave amplitude can be increased by using different forcing mechanisms [8]. Quite generally, stable continuously stratified fluids support internal wave beams resulting from a disturbance in the fluid [3, 20, 18, 17, 4]. The properties of internal gravity waves in laboratory experiments have often been observed and measured using schlieren [15] and more recently synthetic schlieren [2, 18] techniques. Synthetic schlieren observations provide an integrated view and usually assume homogeneity of the fluid response in the direction of view, as if it were two-dimensional. These observations are sensitive to the gradient of the density perturbation, but it is possible to invert this to recover the perturbation density (see [2] and in a simpler form in [18]). However, it has become customary to present just the directly observed gradient information rather than the more natural density perturbation itself. By its very design, PIV (particle image velocimetry) leads to planar velocity measurements in the fluid. Again assuming homogeneity in one direction, the measured velocity fields can be combined in streamfunction ψ. The streamfunction relates the velocity fields, $(u, w) = (-\psi_z, \psi_x)$ (where we anticipate that in the following u will be the velocity component in the horizontal x direction and w the velocity in the vertical z direction). This streamfunction is also the field considered in the theory for internal wave attractors [13, 10].

The laboratory experiments of Hazewinkel et al.[7] were very successfully modelled in a numerical study [5] using the MIT general circulation model [14] in a two-dimensional set-up. Naturally, the calculations were done in terms of the density field, but, in order to compare with the observation from the laboratory, the gradient density fields were presented. The very strong correspondence between the results of laboratory and numerics allows for further comparison. It suggests that indeed the laboratory experiments can be assumed two-dimensional. If this is confirmed, the use of the streamfunction makes sense and wider connection can be made between theory and observations. The use of numerical simulation and laboratory experiment can then answer the open question as to what is the streamfunction of internal wave attractors is in a real viscous fluid.

Theoretically, the two-dimensional inviscid streamfunction for free internal waves in an enclosed domain with suitably re-scaled coordinates, can be found exactly by solving the spatial wave equation

$$\frac{\partial^2 \psi}{\partial x^2} - \frac{\partial^2 \psi}{\partial z^2} = 0, \tag{1}$$

with $\psi = 0$ at the arbitrarily shaped boundaries, by means of ray tracing [13]. The equation can be solved by noting that an arbitrary complex function f is preserved along the characteristics $x - z$ and $x + z$. From any starting point at the surface the characteristics reflect through the domain, creating a web of connected points. Once the web is constructed, the prescription of f at the surface determines the spatial structure of $\psi(x, z)$. However, as f is preserved along the rays, there are connections between surface points. This means that the surface prescription of f should be limited to so-called fundamental intervals. This localised prescription then determines the structure of $\psi(x, z)$ in the whole domain. An example of such a streamfunction for a rectangular tank with a sloping side wall (trapezoid) was presented by [12], see figure 1a. This geometrically constructed, unforced internal wave pattern is self-similar in space and has fine structures around the attractor, set only by the form of f across the fundamental intervals at the surface. The corresponding analytic solution for streamfunction recovers these fine structures and features a self-similar spectrum [11]. A modified picture for the streamfunction was found [9] for a continuous forcing in the form of seiche wave at the surface. In order to preserve this continuous pressure along the surface it was assumed that the imposed values did not influence surface pressure values elsewhere, even though the points were connected by the characteristics. The modified picture for the streamfunction, although still inviscid, lost most of the fine structure. It became more a plateau type, that is, the streamfunction has constant values outside and inside the attractor with a sharp jump in value at the attractor, see figure 1b. Similar solutions for the streamfunction were found in numerical work, using a regularisation procedure for the discretised problem, based on minimisation of the energy [19].

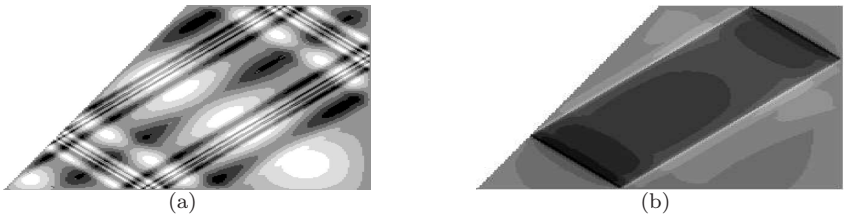

(a) (b)

Figure 1: Streamfunction for inviscid internal wave attractor as found by [12] and [9]. a) A free wave solution, b) the forced wave solution. [Courtesy Frans-Peter Lam]

The objectives of this paper are twofold. Building further on the successful two-dimensional numerical simulation of the laboratory experiments [5], we now compare results from laboratory and simulation that both feature a tank scale sloshing as internal wave forcing. First we use the numerically obtained density field to verify the integration of the density gradient fields observed in the laboratory, and use this field to check if two-dimensional theory applies in the laboratory experiment. Secondly, we compare the observed streamfunction from both laboratory experiments and from numerical experiments with the prediction from two-dimensional theory for a sloshing type of forcing.

2. Experimental setup

Fluid height	H	=	250	mm
Length	L	=	453	mm
Width (Lab)	W	=	120	mm
Angle of sloping wall	α	=	0.47	rad
Buoyancy frequency	N	=	2.2±0.1	rad s^{-1}
Viscosity	ν	=	1	$mm^2 s^{-1}$
Diffusivity	κ	=	1.3×10^{-3}	$mm^2 s^{-1}$
Prandtl number	$Pr = \nu/\kappa$	=	770	
Forcing period	T	=	$5.12 \pm 5 \times 10^{-3}$	s
Forcing frequency	$\omega_e = 2\pi/T$	=	1.23	rad s^{-1}

Table 1: Parameters of both experiments §2.

2.1. Description of laboratory experiments

For the laboratory experiments a trapezoidal tank containing a fluid with dimensions $L \times W \times H$ is used, see table 1. As the tank is relatively narrow, the motion was assumed to be nearly two-dimensional in previous work. The tank is filled using a pair of peristaltic pumps with density stratification that is linear in the vertical. The stratification is characterised by buoyancy frequency $N = \sqrt{-g/\rho_0 \; d\bar{\rho}/dz}$ with ρ_0 the reference density of the fluid, $\bar{\rho}(z)$ the density stratification and g the acceleration due to gravity. We use a density probe that can traverse vertically through the tank to establish N. To measure the motions of the fluid in the tank, we make use of both synthetic schlieren and PIV techniques, as described in [8, 6]. For the synthetic schlieren, we have a dot pattern on a light-bank 0.5 m behind the tank fixed in the laboratory. The internal waves are forced by horizontally oscillating a platform supporting the tank with an amplitude of 2 cm at fixed frequency ω. This horizontal motion of the platform results in a weak sloshing of the water in the tank. The sloping side wall converts this barotropic sloshing into weak baroclinic internal waves that focus towards the attractor to form wave beams [7]. As the tank and fluid are horizontally oscillating in front of the dot pattern, we phase lock the camera with the oscillation, capturing 32 frames evenly spaced through each forcing period. This allows us to perform the synthetic schlieren during the steady state of the experiment, with each of the 32 snapshots having its own reference frame to remove the influence of any optical imperfections in the tank. The particles for the PIV are Iriodin Glitter Bronze 530 from which we selected fine particles that slowly sink out in the fluid. The images used for the PIV are captured using the same phase-locked technique as for the synthetic schlieren. Both synthetic schlieren and PIV techniques rely on pattern matching. In the case of synthetic schlieren, the dot pattern gets distorted by density and hence refractive index changes in the fluid. The apparent displacement of the dots due to this distortion is determined by correlation with an unperturbed image. For

the PIV, the particle patterns from frame to frame are tracked and represent the local Eulerian velocity field (though the particles are Lagrangian of course). The data are analyzed with the DigiFlow software (Dalziel Research Partners, Cambridge). For simplicity and to maximise the signal quality, we used separate experiments for the synthetic schlieren and PIV measurements. This was possible as the experiments proved to be highly repeatable, with differences of less than 3% even after emptying and refilling the tank. Typically, we used a given stratification twice, first for synthetic schlieren then, after adding particles, for PIV, further reducing the difference in the conditions between SS and PIV runs.

2.2. Description of numerical simulation

The numerical configuration is nearly the same as in [5]. The MIT general circulation model is used in a two-dimensional configuration to solve the nonlinear, nonhydrostatic, incompressible Boussinesq equations that govern the fluid dynamics [14]. Its second-order finite volume implementation allows for a simple treatment of the topography (as opposed to spectral methods). No sub-grid parametrization is used and the simulation models diffusion using the ordinary Laplacian operator. They are at a high enough resolution to ensure the motion is well resolved. Indeed, the spatial resolution $\triangle$ is 0.5 mm in both vertical and horizontal directions, meaning that the width of the attractor ($\sim$ 5 cm) is resolved by about hundred points. For technical reasons regarding the way the code handles the equations, the numerical domain and the vertical density gradient are flipped in the z-direction relative to those of the experiments. The Boussinesq equations are indeed invariant under this transformation and to keep the comparison simple, the figures related to the numerical simulation will be flipped again in the z-direction. We discretise time into 250 time steps per forcing period. The fastest wave propagating in the domain being the mode-one internal wave of horizontal phase speed $H\sqrt{N^2-\omega_e^2}/\pi$, the Courant number in our configuration is therefore

$$C = \frac{H\sqrt{N^2T^2 - 4\pi^2}}{250\pi\triangle} \approx 6$$

The physical parameters are based on those used in the laboratory experiment and are listed in table 1. The numerical physical setting is nearly the same as in the laboratory, although some discrepancies remain. A first difference lies in the forcing that is of a different nature than the forcing in the laboratory one. Indeed, in the laboratory experiment the horizontal velocity of the fluid vanishes (relative to the tank) at the vertical wall, whereas for the numerical simulation we use an open boundary condition in the form of an oscillating current (u_b, w_b) at the vertical wall, reproducing a mode-1 internal wave:

$$u_b(t,z) = \frac{A\sqrt{N^2-\omega_e^2}}{N}\sin(\omega_e t)\cos\frac{\pi z}{H}$$
$$w_b(t,z) = -\frac{A\omega_e}{N}\cos(\omega_e t)\sin\frac{\pi z}{H}$$

The amplitude of the mode-one wave, $A = 0.4\,\mathrm{mm/s}$, is chosen so that the maximal velocity within the attractor field is in close agreement with the experimental one, which is the order of $10\,\mathrm{mm/s}$. Another difference lies in the purely two-dimensional numerics that cannot take into account the dissipation that occurs in viscous shear layers at the front and back walls in the laboratory experiment. The long horizontal side of the trapezium, which is located at the bottom of the experiment but at the top of the numerical domain, is coded with a linear free-surface condition. A free-slip boundary condition is implemented for the short horizontal side (which is located at the bottom of our numerical domain) and the sloping boundary of the trapezium in order to inhibit viscous layers that would be underresolved. Indeed, the Reynolds number is higher where the beams reflect against boundaries. With a typical fluid velocity of $1\,\mathrm{cm/s}$, a typical scale of $50\,\mathrm{mm}$ and a viscosity ν as defined, the Reynolds number there is about 500, low enough for the boundary layer to be considered as laminar. The typical thickness of the boundary layer for an oscillating field is $\sqrt{\nu/\omega} \simeq 1\,\mathrm{mm}$, which is too small to be resolved by our grid. As noticed in [5], the absence of viscous effects at the walls might lead to a noticeable underestimation of the dissipation at the boundaries. Finally, the vertical boundary is where the forcing is applied, which is a boundary condition by itself.

A linear equation of state is used and thermal expansion coefficient is chosen such that the stratification is linear in temperature, and thus described by constant N. Thermal diffusivity κ is set to the value for the salt diffusion in the laboratory and no heat flux is prescribed at the boundaries.

2.3. New method of representing experimental data

In most previous work the results of the synthetic schlieren imaging are presented in terms of the gradient perturbation buoyancy fields [21, 1], $(b_x, b_z) = -g/\rho_0 \nabla \rho'$, as these are directly found from the distortions of the dot pattern by density perturbation ρ'. Here, we introduce the integrated field

$$b = \nabla^{-1}(b_x, b_z). \tag{2}$$

Although we expect $b = \nabla^{-1}(b_x, b_z)$, direct integration is complicated by noise in the experimental measurements of the irrotational ∇b field, leading to an additional rotational part. We thus choose to integrate $b = (g/\rho_0)\rho'$ through a least squares procedure that minimises the energy contained in the rotational part, see the Appendix for details. In summary, we note that the least squares solution for b on a regular two-dimensional grid with an irregular boundary, for each point in the domain or on the boundary, corresponds to taking the mean of the solutions calculated from the (up to four) immediately neighbouring points at which the solution exists. The structure of this problem then leads itself to a simple iterative solution, convergence of which is greatly enhanced by formulating in a multigrid framework. Only a single arbitrary constant of integration is required, here selected so that the spatial mean of b vanishes. We note in passing that setting $b = 0$ outside the domain and then using the regular procedure (e.g. using library function intgrad2 [John D'Errico, Mathworks]) for

integrating the gradient in a rectangular domain leads to a slightly larger error, but provides a good alternative. The main problem points are found to be the sloping wall and the reflection points at the walls and surface. However, the difference fields, $b_{x,z} - \nabla(\nabla^{-1}(b_x, b_z))$ are at most 5% in the reflection points and much smaller elsewhere.

We can use the same multigrid least squares iteration procedure to determine the streamfunction from

$$\psi = \nabla^{-1}(w, -u), \tag{3}$$

effectively minimising the energy of the non-solenoidal part of the measured (u, w).

Two-dimensional linear internal wave theory relates the buoyancy b with the vertical velocity. This is readily understood since, in the absence of diffusion, the density surfaces move up and down with the vertical velocity. The relation,

$$b = -i\frac{N^2}{\omega}\psi_x, \tag{4}$$

allows for another check on the integration: a check that ought to be included whenever velocity and buoyancy fields are measured separately. In the numerical simulation this relation is fully recovered, as expected from the two-dimensional code. In the laboratory experiment it provides both a check whether our integration of the buoyancy field works, and a validation of our assumption that we measure an essentially two-dimensional field. This assumption underlies most of the previous work on attractors in narrow tanks [12, 7, 8, 6] and practically all previous experimental studies to internal waves.

3. Results

For the parameters used in the laboratory, the density gradient fields reveal a simple, essentially rectangular attractor with a shape very similar to that presented by previous authors [7, 5]. From the PIV observations, we find the accompanying velocity fields. The forcing is somewhat stronger than that used by [7, 5], giving shear velocities in the attractor branches that are an order of magnitude larger, i.e. 10 mms^{-1}. The velocity fields in the laboratory are poorly resolved in places, due to the combination of low seeding densities (particularly under the sloping boundary), and the wave-driven net-drift of PIV-tracers [6] (this net-drift eventually results in a weak three-dimensional flow).

We observe the growth of an attractor in about twenty periods, featuring the generation of low-wavenumber internal wave beams from the sloping wall and the subsequent focussing, linear wavenumber cascade, towards the attractor. The wavenumber spectrum achieves a steady state once the high-wavenumber side of the spectrum reaches the dissipation length-scale. From this steady state we obtain the perturbation gradient density fields and velocity fields. The experiments were forced during 50 periods.

We calculate the density perturbation field by integrating the gradient fields measured by synthetic schlieren and then perform harmonic analysis on the integrated fields over the last twenty periods. The resulting perturbation density field is compared with the harmonic analysis of the perturbation density from the numerical simulation. From the harmonic analysis we obtain a real and an imaginary part that are combined to one complex field, so that we can plot both the amplitude and phase of this complex field. Amplitude and phase show the imprint of the attractor, visible in figure 2. The amplitude field reveals a decay in the clockwise direction of the branches (the internal wave beams) from the sloping wall. Compared with the numerical simulation, the cross-sections of the attractor branches are wider in the experiment but the values are comparable. The same difference in confinement is observed in structure of the phase. Although values are in agreement, the angle of propagation in the laboratory experiment is different in the upper and lower part of the fluid. This indicates a non-constant N and results in an attractor that looks a bit different.

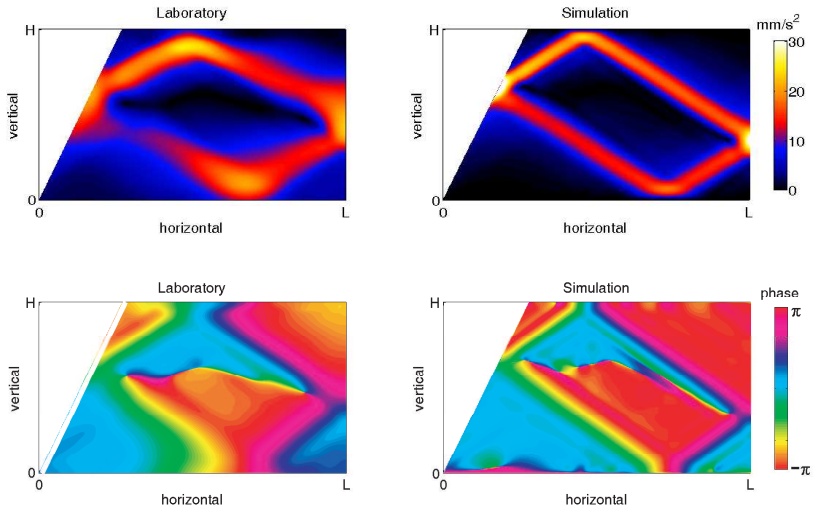

Figure 2: The amplitude and phase of the perturbation buoyancy after harmonic analysis. Laboratory on the left and numerical model on the right

Figure 3 uses relation 4 to compare the buoyancy field from the integrated synthetic schlieren data and the vertical velocity component from the PIV. As the synthetic schlieren and PIV measurements are performed separately, we leave out the phase part (the -i in equation 4), instead we compare absolute values. The structure of both fields is very similar, apart from the region under the slope where we cannot measure the velocity. Where both measurements exist, the values differ by less than 5%.
As for the density, from harmonic analysis we obtain real and imaginary com-

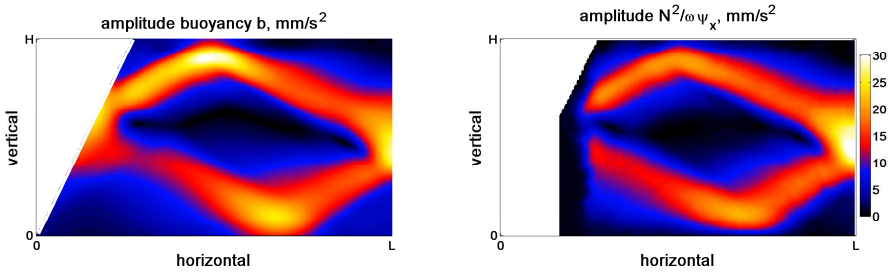

(a) (b)

Figure 3: Comparison between observed a) buoyancy field amplitude and b) vertical velocity field via left-hand side and right-hand side in equation 4.

ponents for vertical and horizontal velocity fields. These are integrated to provide the complex amplitude of the streamfunction (and can be combined to the complex streamfunction field). We do this for both numerical simulation and laboratory experiment and the show real part in figure 4. The actually measured velocities and the derivative of ψ differ less than 1%. The observed streamfunctions are similar but again show, as would be expected, the different angle of propagation. They both reveal that a realistic streamfunction field is of simple shape. The numerical simulation results in somewhat lower values due to the more confined structure of the velocity field.

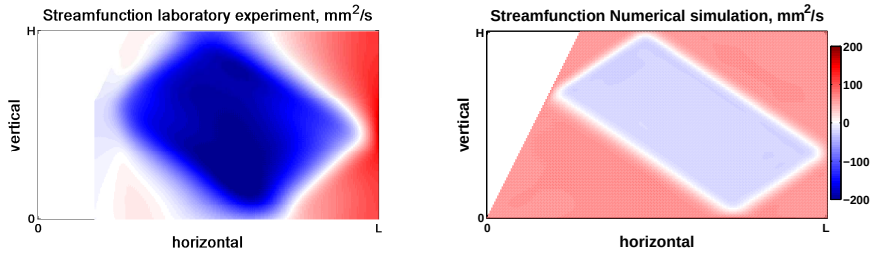

(a) (b)

Figure 4: Streamfunction for a) experiment and b) numerical simulation.

4. Discussion and summary

The qualitative agreement between gradient density fields in the laboratory and from the numerical simulation was reported previously [5]. Here, we conclude that the numerical simulation and the laboratory experiment also correspond quantitatively notwithstanding some distinct differences between them. The

observed density fields have similar amplitude values and phase structure. The forcing in the numerical simulation is adjusted such that the peak velocities correspond to the peak velocities observed in the laboratory experiment. This does not mean the streamfunction values will match, only that the peak gradients in the streamfunction will match. In particular, given the difference in spatial structure, the range of streamfunction values will be greater for the experiments, as is indeed the case. The difference in propagation angle of the wave beams in numerical and laboratory experiment is related to our uncertainty about the stratification in the laboratory experiment, that features a slightly non-constant value of N.

The differences in spatial structure found between the two suggest that considering only internal dissipation of the waves is not realistic. As the dissipation from the front and back wall in the laboratory is likely to affect only the low wave numbers, it seems that the boundary layers where reflections occur are important in the laboratory experiment. The top and bottom of the fluid in the laboratory feature some mixed layers, as can be seen from the phase spreading at those locations in figure 2.

The use of the streamfunction is only possible in a two-dimensional description of the flow. In our comparison, we recognise that the numerical simulation is two-dimensional and that the laboratory is not. This may explain some further differences in the spatial structure of the streamfunction. However, the accurate recovery of the relation between observed buoyancy and vertical velocity reveals that the laboratory experiments are well described by two-dimensional theory (figure 3). This two-dimensionality is something that should be tested in laboratory observations whenever both synthetic schlieren and PIV data are available. The streamfunction fields are the plateau type of solution, very comparable to the solutions found for a sloshing forcing at the surface. It appears that viscosity smoothes the solution. This is true at least in the smaller laboratory scale where the linear energy cascade of the basin scale waves approaches the viscous scales after a small number of loops [7]. The form of the streamfunction for much larger scale flows (e.g. astrophysical flows) remains an open question [16].

In summary, we presented a new way of working with observations as typically found in laboratory experiments on stratified fluids. The least squares integration of the observed/reconstructed perturbation density gradient fields reveals a physically more readily understood scalarfield, namely the perturbation density field. Comparison with a two-dimensional numerical simulation, and with two-dimensional internal wave theory, reveals that the narrow three-dimensional tank can be considered effectively to be two-dimensional. This effective two-dimensionality also suggests that the description in terms of streamfunction is useful, so the velocity fields are integrated using the same least squares approach to the integration as for the perturbation gradient density fields. Although the streamfunction might arguably be a less physical scalarfield than the perturbation density field, it is the field considered by most theoretical work. We conclude that the streamfunction for a real internal wave attractor in a viscous fluid is of plateau/simple type.

Acknowledgements We thank Leo Maas and Chantal Staquet for comments on an earlier version of this paper and Frans-Peter Lam for help with figure 1. J.H. is supported by a grant from the Dutch National Science Foundation through the NWO/FOM Dynamics of Patterns program. N.G. is supported by a grant from the French Direction Générale de l'Armement (D.G.A) and by the French National Agency for Research (A.N.R) through contract TOPOGI-3D. Numerical experiments were performed on the French supercomputer center I.D.R.I.S, through contract 0705890.

Appendix Inverting density gradients

Let $\boldsymbol{\xi} = (\xi, \zeta)$, the (2D) scaled measurements of the apparent displacement of synthetic schlieren patterns. Without loss of generality, we can write $\boldsymbol{\xi}$ in terms of a scalar potential ρ and vector potential Φ as

$$\boldsymbol{\xi} = \nabla\rho + \nabla \times \Phi. \tag{5}$$

Clearly, $\nabla\rho$ represents the irrotational part of $\boldsymbol{\xi}$, while $\nabla \times \Phi$ is the rotational part. Now since the apparent displacements themselves are due solely to the gradient of a scalar quantity, any rotational part of δ represents an error in the measurement. The segregation of $\boldsymbol{\xi}$ into rotational and irrotational parts, however, is not unique. We might therefore choose to project $\boldsymbol{\xi}$ onto irrotational space to minimise the energy contained in $\nabla \times \Phi$. In particular, we might choose ρ so as to minimise

$$\boldsymbol{\varepsilon} = \int_D (\nabla \times \Phi) d\boldsymbol{x} = \int_D (\boldsymbol{\xi} - \nabla\rho) d\boldsymbol{x}, \tag{6}$$

where ε is the energy in the rotational field and D is the fluid domain. The synthetic schlieren measurements $(\xi_{i,j}, \zeta_{i,j})$ are obtained on a regular grid $(x_i, y_j) = (i\triangle, j\triangle)$, with $i = [0, m]$ and $j = [0, n]$, so it is convenient to consider a discrete version of 6. For reasons which shall become clear, we elect to form the discrete version using central differences on a staggered grid with spacing $\triangle$,

$$\boldsymbol{\varepsilon} = \Sigma_{i=0}^{m-1}\Sigma_{j=0}^{n}(\xi_{i+\frac{1}{2},j} - \frac{\rho_{i+1,j} - \rho_{i,j}}{\triangle})^2 + \Sigma_{i=0}^{m}\Sigma_{j=0}^{n-1}(\zeta_{i,j+\frac{1}{2}} - \frac{\rho_{i,j+1} - \rho_{i,j}}{\triangle})^2, \tag{7}$$

where we use linear interpolation to determine $\xi_{i+\frac{1}{2},j} = (\xi_{i+1,j} + \xi_{i,j})/2$ and $\zeta_{i,j+\frac{1}{2}} = (\zeta_{i,j+1} + \zeta_{i,j})/2$. This summation is rewritten as

$$\boldsymbol{\varepsilon} = (\delta - M\rho)^T(\delta - M\rho) \tag{8}$$

where δ is a vector containing $P = m(n+1) + n(m+1)$ entries serialising the $m(n+1)$ values of $\xi_{i+1/2,j}$ and the $n(m+1)$ values of $\zeta_{i,j+1/2}$, and $\boldsymbol{\rho}$ contains the $Q = (m+1)(n+1)$ (unknown) serialised $\rho_{i,j}$ values. The $P \times Q$ matrix M is block bi-diagonal, zero apart from entries of $1/\triangle$ along the diagonal and $-a/\triangle$ somewhere else along the same row (with the position depending on whether the row represents an x or z gradient).

Since $P > Q$ then the system is over-determined and minimising ε is a least squares problem, the solution of which requires ρ to be chosen such that

$$M^T M\boldsymbol{\rho} = M^T\boldsymbol{\delta} \tag{9}$$

While this linear problem can be solved directly (e.g. using Singular Value Decomposition or the Householder Transformation), this calculation is computationally expensive. However, the particular structure of $M^T M\boldsymbol{\rho}$ and $M^T\boldsymbol{\delta}$ reveals an alternative approach. In particular, we note that for internal points we have

$$\frac{\rho_{i+1,j} + \rho_{i-1,j} + \rho_{i,j+1} + \rho_{i,j-1} - 4\rho_{i,j}}{\triangle^2} = \frac{\xi_{i+1,j} - \xi_{i-1,j} + \zeta_{i,j+1} - \zeta_{i,j-1}}{2\triangle}, \tag{10}$$

the second order finite difference approximation to $\nabla^2\rho = \nabla \cdot \boldsymbol{\xi}$. At boundary points the formula is similar, omitting values that fall outside the domain. For example, at the $i = 0$ boundary (away from the corner),

$$\frac{\rho_{i+1,j} + \rho_{i,j+1} + \rho_{i,j-1} - 3\rho_{i,j}}{\triangle^2} = \frac{(\xi_{i+1,j} + \xi_{i,j}) + \zeta_{i,j+1} - \zeta_{i,j-1}}{2\triangle}, \tag{11}$$

while when we also have $j = n$ (hence a corner point) this further reduces to

$$\frac{\rho_{i+1,j} + \rho_{i,j+1} - 2\rho_{i,j}}{\triangle^2} = \frac{(\xi_{i+1,j} + \xi_{i,j}) - (\zeta_{i,j} + \zeta_{i,j-1})}{2\triangle}, \tag{12}$$

The brackets on the right-hand side in these last two expressions serve to highlight the role played by the interpolated values $\xi_{i+1/2,j}$ and $\zeta_{i,j-1/2}$. The simplicity of the above expressions, and the similarity between these and the Poisson equation, has two important consequences. First, an iterative solution using a multigrid formulation is both straight forward and efficient. Second, the multigrid solution is readily adapted for more complex domains. The relaxation step of the multigrid is essentially replacing $\rho_{i,j}$ with the mean value obtained using the trapezium integration rule from each of the surrounding points that fall within the domain. Indeed, although not formulated as a least squares problem, this natural approach to direct iterative integration of the observed density gradient is exactly what has been used previously by [2].

References

[1] Dalziel, S. B., Carr, M., Sveen, J. K., Davies, P. A., Mar. 2007. Simultaneous synthetic schlieren and PIV measurements for internal solitary waves. Meas. Sci. Technol. 18, 533–547.

[2] Dalziel, S. B., Hughes, G. O., Sutherland, B. R., 2000. Whole-field density measurements by 'synthetic schlieren'. Exp. Fluids 28, 322–335.

[3] Goertler, H., 1943. Über eine Schwingungserscheinung in Flüssigkeiten mit stabiler Dichteschichtung. Z. angew. Math. Mech. 23, 65–71.

[4] Gostiaux, L., Dauxois, T., Didelle, H., Sommeria, J., Viboud, S., May 2006. Quantitative laboratory observations of internal wave reflection on ascending slopes. Phys. Fluids 18 (5), 056602–+.

[5] Grisouard, N., Staquet, C., Pairaud, I., Nov. 2008. Numerical simulation of a two-dimensional internal wave attractor. J. Fluid Mech. 614, 1–14.

[6] Hazewinkel, J., Dalziel, S. B., Doelman, A., Maas, L. R. M., 2010. Tracer transport by internal wave beams., unpublished, see J. H.'s homepage.

[7] Hazewinkel, J., van Breevoort, P., Dalziel, S. B., Maas, L. R. M., Mar. 2008. Observations on the wavenumber spectrum and evolution of an internal wave attractor. J. Fluid Mech. 598, 373–382.

[8] Hazewinkel, J., van Breevoort, P., Doelman, A., Maas, L. R. M., Dalziel, S. B., Dec. 2007. Equilibrium spectrum for internal wave attractor in a trapezoidal basin. In: Proceedings of the 5th International Symposium on Environmental Hydraulics.

[9] Lam, F.-P. A., Maas, L. R. M., Feb. 2008. Internal wave focusing revisited; a reanalysis and new theoretical links. Fluid Dyn. Res. 40, 95–122.

[10] Maas, L. R. M., 2005. Wave attractors: linear yet nonlinear. Int. J. Birfurcat. Chaos 15, 2757–2782.

[11] Maas, L. R. M., Mar. 2009. Exact analytic self-similar solution of a wave attractor field. Physica D 238, 502–505.

[12] Maas, L. R. M., Benielli, D., Sommeria, J., Lam, F.-P. A., Aug. 1997. Observation of an internal wave attractor in a confined, stably stratified fluid. Nature 388, 557–561.

[13] Maas, L. R. M., Lam, F.-P. A., 1995. Geometric focusing of internal waves. J. Fluid Mech. 300, 1–41.

[14] Marshall, J., Adcroft, A., Hill, C., Perelman, L., Heisey, C., 1997. A finite-volume, incompressible Navier Stokes model for studies of the ocean on parallel computers. J. Geophys. Res. 102, 5753–5766.

[15] Mowbray, D. E., Rarity, B. S. H., Apr. 1967. A theoretical and experimental investigation of the phase configuration of internal waves of small amplitude in a density stratified liquid. J. Fluid Mech. 28, 1–16.

[16] Ogilvie, G. I., Oct. 2005. Wave attractors and the asymptotic dissipation rate of tidal disturbances. J. Fluid Mech. 543, 19–44.

[17] Peacock, T., Tabaei, A., Jun. 2005. Visualization of nonlinear effects in reflecting internal wave beams. Phys. Fluids 17 (6), 061702–+.

[18] Sutherland, B. R., Dalziel, S. B., Hughes, G. O., Linden, P. F., Jul. 1999. Visualisation and measurement of internal waves by synthetic schlieren. Part 1. Vertically oscillating cylinder. J. Fluid Mech. 390, 93–126.

[19] Swart, A., Sleijpen, G. L. G., Maas, L. R. M., Brandts, J., Mar. 2007. Numerical solution of the two-dimensional Poincare equation. J. Comput. Appl. Math. 200, 317–341.

[20] Thomas, N. H., Stevenson, T. N., 1972. A similarity solution for viscous internal waves. J. Fluid Mech. 54, 495–506.

[21] Yick, K.-Y., Stocker, R., Peacock, T., Jan. 2007. Microscale Synthetic Schlieren. Exp. Fluids 42, 41–48.